Journal of the Korean Nuclear Society
Volume 28, Number 1, February 1996

Spacer Grid Effects on Turbulent Flow in Rod Bundles

Sun Kyu Yang and Moon Ki Chung
Korea Atomic Energy Research Institute
(Received September 7, 1995)

지지격자가 봉다발 난류유동에 미치는 영향

양선규 · 정문기
한국원자력연구소
(1995. 9. 7 접수)

Abstract

The local hydrulic characteristics in subchannels of 5×5 nuclear fuel bundles with spacer grids were measured at upstream and downstream of the spacer grid for the investigation of the spacer grid effects on turbulent flow structure by using an LDV(Laser Doppler Velocimeter). The measured parameters are axial velocity and turbulent intensity, skewness factor, and flatness factor. Pressure drops were also measured to evaluate the loss coefficient for the spacer grid and the friction factor for rod bundles. From these data, it was found that the turbulent mixing and forced mixing occur up to $x/D_h = 10$ and 20 from the spacer grid, respectively. The turbulence decay behind spacer grid behaves in the similar decay rate as turbulent flow through mesh grids or screens. Mixing factors useful in subchannel analysis code were correlated from the data and show the highest value near spacer grid and then have a stable values.

요 약

지지격자를 갖는 5×5 핵연료 봉다발부수로내에서 국부 수력특성인자들을 레이저 유속측정장치인 LDV(Laser Doppler Velocimeter)를 이용하여 측정하였다. 이 연구는 지지격자가 봉다발 난류유동구조에 미치는 영향에 관한 연구에 관점을 두었다. 축방향속도, 난류강도, 편이도, 편평도 등의 측정인자들을 측정하였다. 압력강하를 측정하여 지지격자의 손실계수와 봉다발의 마찰계수를 구하였다. 실험결과로부터 활발한 난류혼합거리는 지지격자로부터 $x/D_h = 10$까지이고, 강제 혼합거리는 지지격자로부터 $x/D_h = 20$까지임이 관찰되었다. 지지격자하류에서의 축방향 난류강도 감쇄거동은 mesh격자나 screen을 통과하는 난류유동과 같은 경향을 보여주었다. 측정된 자료로부터 부수로해석 code에 입력함수로 적용할 수 있는 국부 난류혼합계수상관식을 구하였다. 국부 혼합계수분포 경향을 관찰하여보면 지지격자 근처에서 최대값을 보이고, 하류방향으로 진행하면서 안정된 값을 갖는다.

1. Introduction

Research on the turbulent flow characteristics of the fuel assembly with spacer grids is of importance for thermal hydraulic design and safety analysis. This study is focused on turbulent structure modulation due to spacer grids in a 5×5 rod bundle which is a scale-downed geometry of the fuel full-assembly. The roles of the spacer grid are to support the rods regularly and to promote flow mixing which in turn enhances thermal mixing. The spacer grid tested in the present work is a mixing spacer grid with mixing vanes.

Major features of turbulent phenomena in subchannels include cross-flow mixing between subchannels [1], anisotropy of turbulent diffusion[2−4], and secondary flow[5]. They are illustrated in Fig. 1. In addition to these turbulent phenomena, there is drastical turbulence generation near spacer grid which is caused by the sharp edge and blockage of spacer grid. Generated turbulence due to spacer grid decreases rapidly as the flow develops. In this study, turbulence decay behind spacer grids and cross-flow mixing phenomena between subchannels were investigated more in detail. There are two kinds of cross-flow mixing mechanisms in rod bundle flow: macroscopic mixing, which is due to the time mean lateral or azimuthal velocity, and microscopic turbulent mixing, which is caused by fluctuating velocity. In particular, the present work focuses on the microscopic turbulent mixing between neighboring subchannels, which is related to the turbulent thermal mixing.

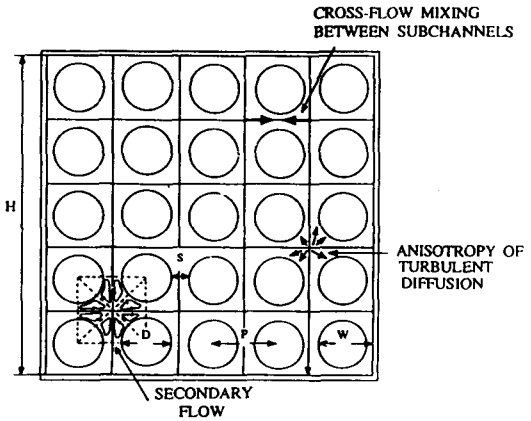

Fig. 1. Turbulent Phenomena in Subchannels

Previous experimental studies on the flow characteristics near spacer grids in bare rod bundles include Rehme[6], Rowe and Chapman[7], Rehme and Trippe[8], and Shen et al.[9]. Rehme[6] measured the pressure drops for the various kinds of the spacer grids. An experimental study by Rowe and Chapman[7] was carried out to evaluate the effect of spacer grids on the axial turbulent flow structure in rod bundles. Local axial velocity and turbulent intensity were measured upstream and downstream of spacer grids by using a LDV(Laser Doppler Velocimeter). The highest intensity was observed downstream near the spacer grid and decayed rapidly to stable value far downstream. However, they could not give information on the correlations for the turbulence behind spacer grids and for local mixing factors. And higher moments of turbulent fluctuations were not measured. Compared to Rowe and Chapman, in the present work, more detailed measurements for new turbulent parameters in axial locations were performed upstream and downstream of spacer grids, which gave information of the spacer grid effects on turbulent flow structure quantitatively. Rehme and Trippe measured, by using Pitot tubes, in detail the velocity distributions upstream and downstream of spacer grids. The mass flow separation and redistribution between the subchannels are discussed and compared with the prediction by a subchannel code. Shen et al. performed detailed measurements using LDV in water to obtain information on the distribution of the transverse mean velocity and turbulent intensity for a flow through a sixteen-rod bundle with mixing blades on the spacer grid. They observed that the mixing rate varies largely with the angle of mixing blade on the spacer grid.

In this study, the detailed hydraulic characteristics of the turbulent flow through mixing spacer grids in

5×5 rod bundles were measured by using an LDV. The measured parameters include pressure drops, axial velocity and turbulent intensity, skewness factor, and flatness factor. Loss coefficients for the spacer grid and friction factors for rod bundles were estimated from the measured pressure drops. Implications regarding the turbulent thermal mixing caused by spacer grids were investigated.

2. Experimental Method

2.1. Test Facility

The tested 5×5 spacer grid is shown in Fig. 2.

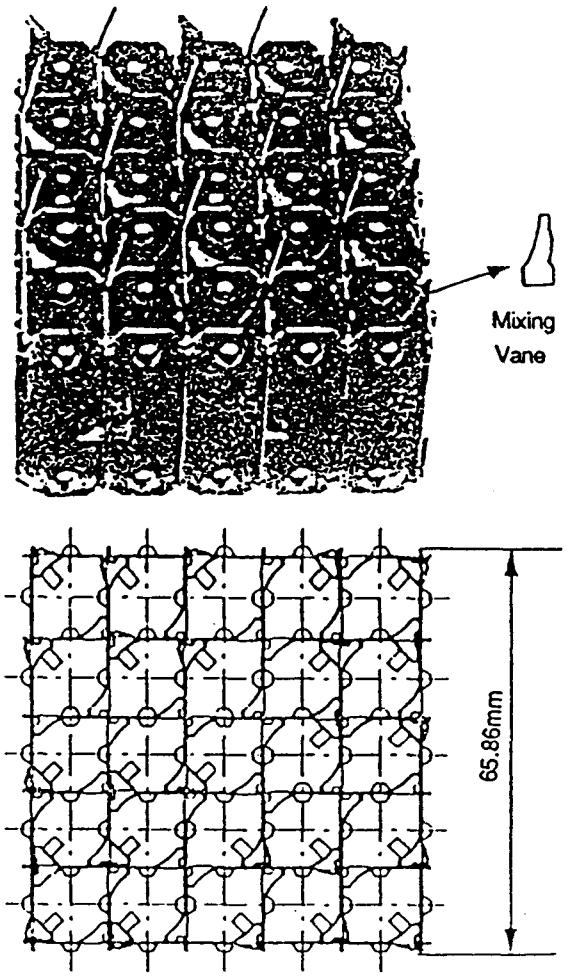

Fig. 2. 5×5 Spacer Grid with Mixing Vanes

The mixing vanes are attached on the spacer grid with an angle of 22°C to enhance flow mixing. The test section, as shown in Fig. 3, of 68mm square housing consists of 25 rods of 9.5mm in diameter. The rod bundle forms in a square array with P/D = 1.326 and W/D = 1.4263. The hydraulic diameter(D_h) of the entire channel is 11.21mm. Axial locations of spacer grids and pressure taps are shown in Fig. 4. The mixing spacer grids are positioned in the rod bundle with the span of 600mm. Water is the working fluid. Fluid enters the bottom of the flow housing and flows upward. Test section is set up in test-loop shown schematically in Fig. 5, which includes variable speed pump, a storage tank, flow control valves, and turbine flow meters etc. During the experiments, the water temperature in the test section was maintained at 25°C by adjusting the feed and drain of water in the storage tank. Pressure drops were measured by changing the mass flow rate controlled by variable pump speed and measured by the turbine flow meter. For the turbulent velocity measurement, the flow rate was 14.22 kg/sec resulting in an average flow velocity of 5m/sec and a Reynolds number based on the hydraulic diameter of Re = 62500. The square housing is made of acrylic to allow access for laser

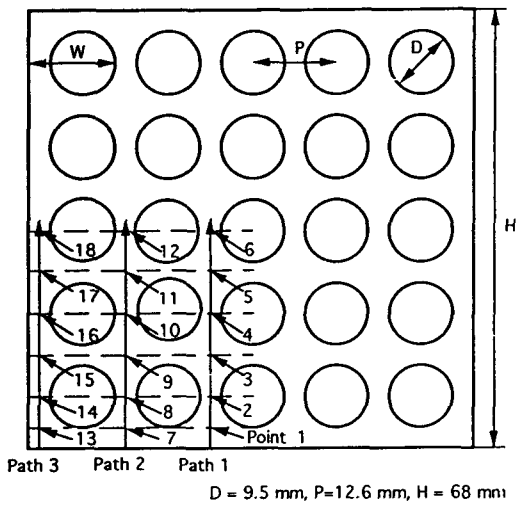

Fig. 3. Cross-Section of 5×5 Rod Bundles and Measuring Location

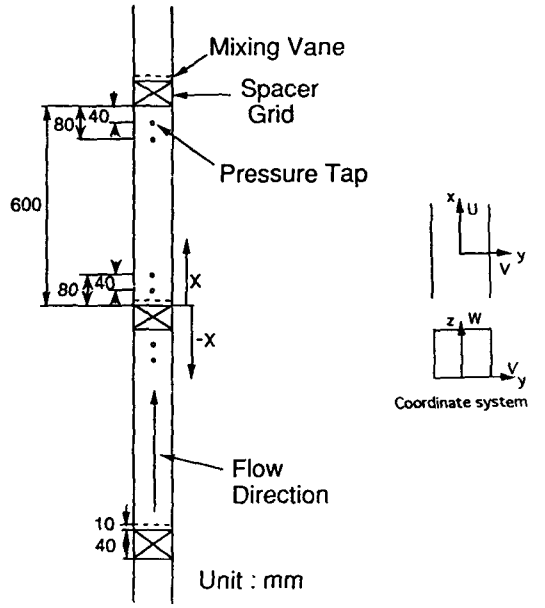

Fig. 4 Axial Location of Spacer Grids and Pressure Taps

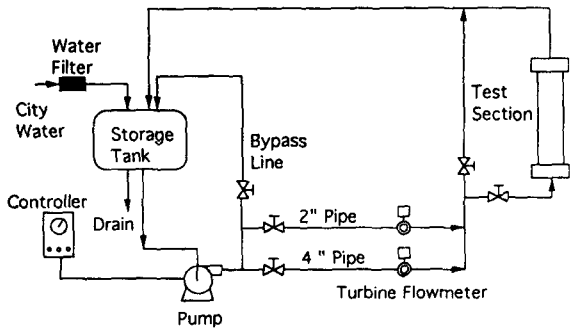

Fig. 5. Flow Diagram of Test Loop

beams to the location where the velocity measurement is to be performed.

2.2. LDV(Laser Doppler Velocimeter)

The LDV measurement method is a non-intrusive optical technique with good spatial resolution, and is based on the principle that coherent laser light scattered from a particle moving with the flow experiences a Doppler frequency shift by an amount directly proportional to its velocity, i.e., to the fluid velocity. The relation between the Doppler shift frequency f_D and the velocity component perpendicular to the optical axis, $\tilde{u}$, is given by

$$f_D = 2\tilde{u}\sin x/\lambda \quad (1)$$

where λ is the laser wavelength and x is the half angle of laser beam intersection[10, 11]. The one-component He-Ne LDV system from TSI, which is used in the present work, was aligned by the dual-beam backward scattered mode as shown in Fig. 6. The dual beam spacing is 50mm and the focal-length of the focusing lens is 250mm.

Silicon carbide particles, 1.5μm in diameter, 3.2 g/cm^3 in density, 2.65 in refractive index, and 1.4 in geometrical standard deviation, were added into the fluid to obtain the scattered signal. The signals from the photomultiplier were processed using a counter type processor which consists of filters, an amplifier, a timer, a digital output, and a D/A(Digital to Analog) converter. The signals from the digital output of the signal processor were used to obtain the turbulent velocity and intensity by using data analysis program FIND from TSI installed in a personal computer. In this software, the correcting process for velocity bias is included. In the present work, since the negative flow was not detected from the prior experiment in our laboratory, frequency shift was not used in the LDV alignment. Minimum measuring distance downstream of spacer was 5mm from the tip of the mixing vane with thickness of 0.48mm. By this thin thickness of the vane, the negative velocity is not existent in the present measuring range.

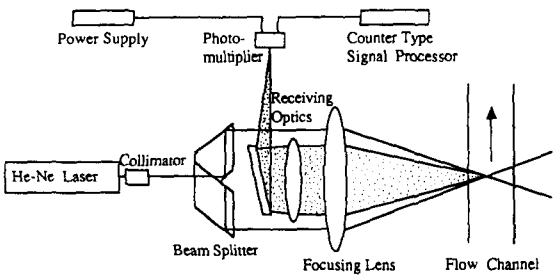

Fig. 6. Backward Scattered Alignment Mode of LDV System

2.3. Measuring Locations

Measuring paths and locations are shown in Fig. 3. and tabulated in Table 1 in accordance with the present coordinate system shown in Fig. 4. Turbulent velocities were measured at Paths 1, 2, and 3 with varying the axial locations (x) in negative and positive direction covering the entire span between spacer grids. Paths are located at central region in gap between rods. At Points on the Paths more detailed flow measurements were performed in particular near spacer grids. Pressure drops were measured at pressure taps shown in Fig. 4.

Table 1. Measuing Locations for 5×5 Rod Bundle Test

coord. Point	x/D_h	y/H	z/H
1	-11~53	0.097	0.06
2	-11~53	0.097	0.13
3	-11~53	0.097	0.22
4	-11~53	0.097	0.31
5	-11~53	0.097	0.41
6	-11~53	0.097	0.50
7	-11~53	0.28	0.06
8	-11~53	0.28	0.13
9	-11~53	0.28	0.22
10	-11~53	0.28	0.31
11	-11~53	0.28	0.41
12	-11~53	0.28	0.50
13	-11~53	0.47	0.06
14	-11~53	0.47	0.13
15	-11~53	0.47	0.22
16	-11~53	0.47	0.31
17	-11~53	0.47	0.41
18	-11~53	0.47	0.50

coord. Point	x/D_h	y/H	z/H
1	2, 4, 8, 16, 32, 50	0.097	0.019~0.54
2	2, 4, 8, 16, 32, 50	0.28	0.019~0.54
3	2, 4, 8, 16, 32, 50	0.47	0.019~0.54

3. Experimental Results and Discussions

3.1. Pressure Drops

The pressure drop at the spacer grid (ΔP_G) is related to the bulk average fluid velocity, U_{av}, in the rod bundle[6].

$$\Delta P_G = C_B \rho \frac{U_{av}^2}{2} \quad (2)$$

where C_B is the loss coefficient of the spacer and ρ is the fluid density. Fig. 7 shows the loss coefficient profile with variation of Reynolds number based on hydraulic diameter and average velocity. Loss coefficients are compared with the reproduced Rehme[6]'s data for the square array with the spacer grid of tube squares axially connected. The present data show lower values than those reported by Rehme.

The friction factors(f) in rod bundles were estimated as shown in Fig. 8 from measured pressure drops and compared with the Blasius[12] correlation

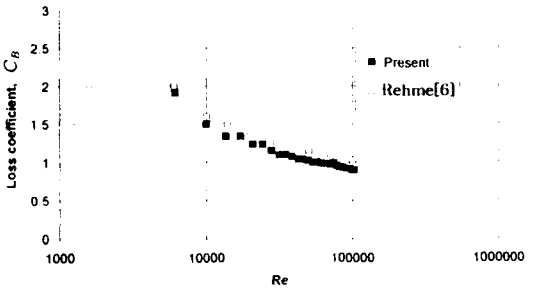

Fig. 7. Loss Coefficients for 5×5 Tests

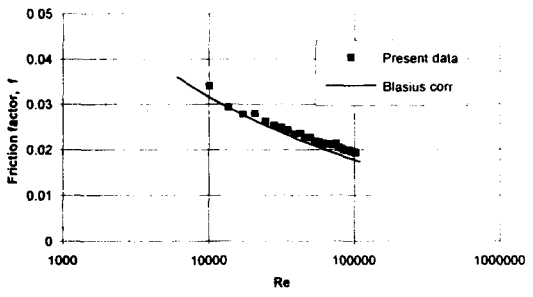

Fig. 8. Friction factors for 5×5 Tests

given by $f=0.316/Re^{0.25}$, where f is Darcy friction factor. The friction factors were estimated as

$$f=-\frac{dP}{dx}\frac{2D_h}{\rho U_{av}^2} \quad (3)$$

The results show that those of the present work are a little higher, about 2.5%, than the values given by the Blasius curve.

3.2. Axial Velocity

Figs. 9~11 show the axially developing velocity profiles at Paths 1~3. The velocitiy profiles at Paths 1 and 2 are similar each other, however, different from that at Path 3 which is in the wall and corner subchannels. The lower spacer grids disturb the local velocity field, which causes a change in mass flow wit hin each subchannel through the spacer grids. Near the upstream spacer grid, at $x/D_h=2$, the flow fluctuates drastically due to the flow blockage and turbulence generation induced by the sharp edge of the spacer grid. At $x/D_h=32$ and 50, the flow is nearly developed. Fig. 12 shows the axial velocity distribution at points 1~6 at different axial locations downstream of spacer grid. The velocities at points 1, 3, and 5 decrease and those at points 2, 4, and 6 increase through spacer grids. Fig. 13 represents the comparisons of the axial velocity distributions at Points 1~18. It is observed that flow mixing occurs intensively after passing through spacer grids up to about

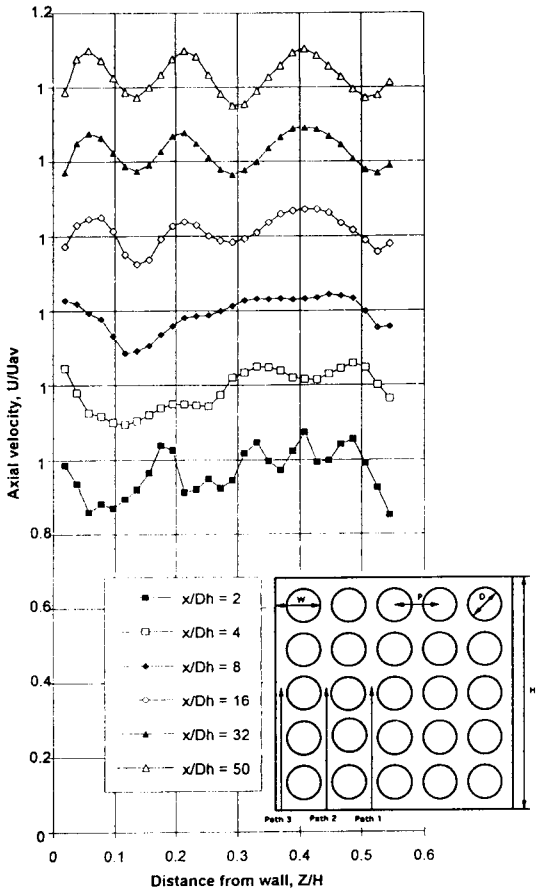

Fig. 9. Developing Axial Velocity at Path 1

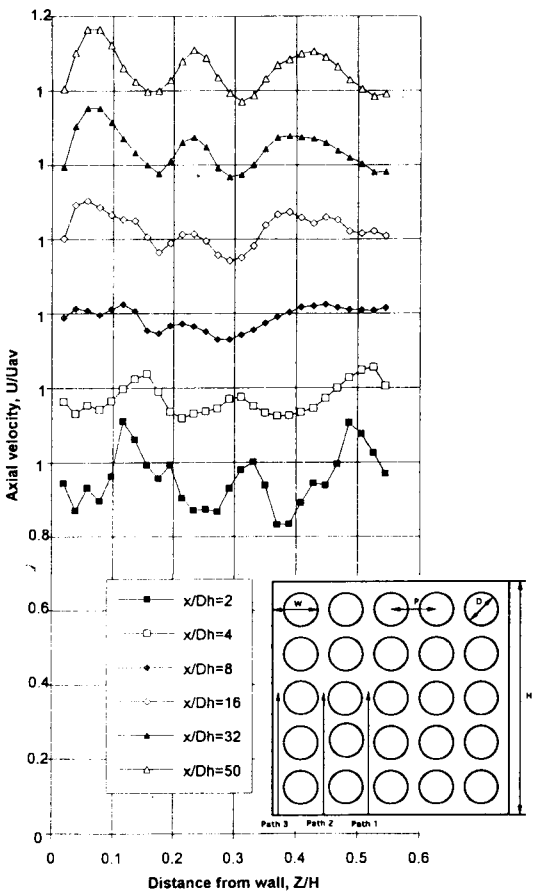

Fig. 10. Developing Axial Velocity at Path 2

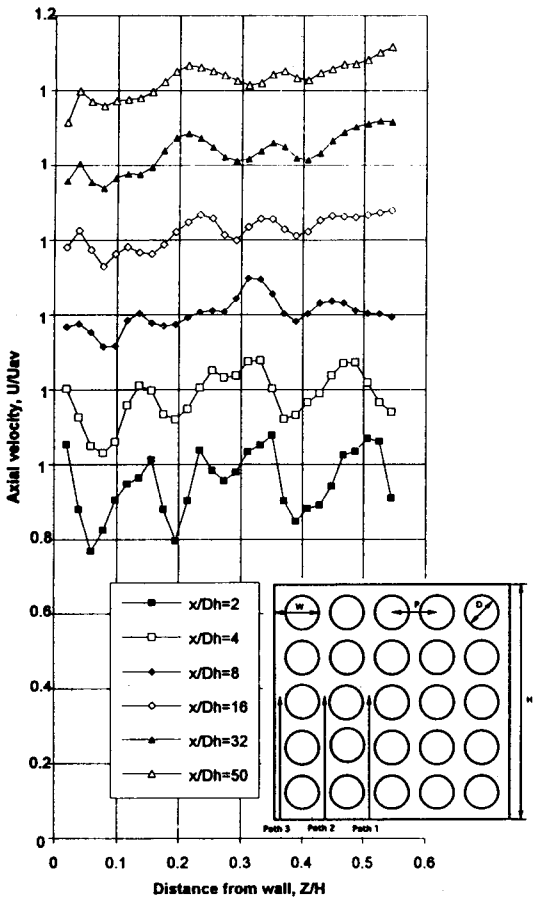

Fig. 11. Developing Axial Velocity at Path 3

$x/D_h = 20$. As the flow develops, the flow distribution become recovered to the original one just before the lower spacer grid.

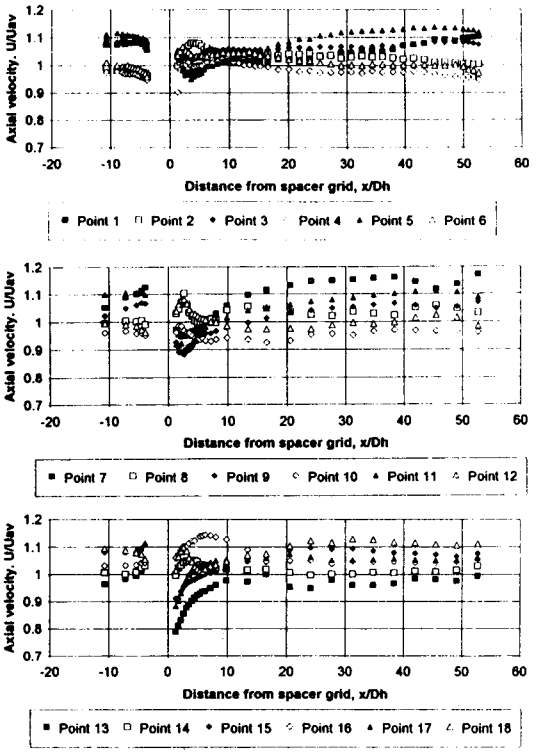

Fig. 13. Axial Velocity Distribution at Points 1~18

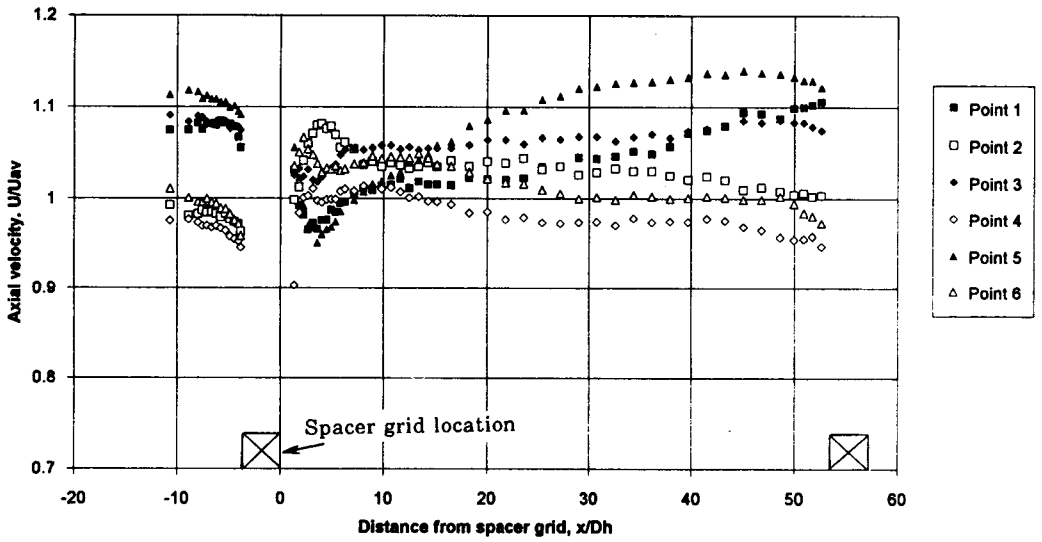

Fig. 12. Axial Velocity Distribution at Points 1~6

3.3. Axial Turbulent Intensity

Fig. 14 is the typical time history of the turbulent velocity for at Point 5 upstream and downstream of spacer grid. Before passing through spacer grids, $x/D_h = -6.24$, velocity fluctuation is small, and after passing through spacer grids, immediately behind spacer grid, $x/D_h = 1.33$, the velocity is fluctuating very intensively. As the flow goes downstream, the fluctuation level becomes to the original one below the lower spacer grid. Fig. 15 represents the axial turbulent intensity distributions at Paths 1~3 in different axial locations. The highest intensity is distributed at $x/D_h = 2$ near the lower spacer grid. The intensities decreases to the lowest value at $x/D_h = 32$ and 50. Axial turbulent intensities at Points are shown in Figs. 16 and 17. Fig. 16 is the turbulent intensity at Points 1~6, showing the spacer grid locations. The turbulent intensity increases drastically through spacer grids, and decreases rapidly to the stable level as the flow develops. Fig. 17 represents the comparisons of axial turbulent intensity at Points. It is observed that the intensities far downstream in the upper grid span coincide excellently with the values far downstream in the lower grid span. This implies that the intensity distributions are repeatable with the grid spans.

The turbulent intensity decay behind the spacer grid can be explained by turbulence decay in turbulent flows through mesh grids[13, 14] or screens[15]. Usually the relation of the turbulence decay rate is expressed as

$$\frac{\overline{u^2}}{U^2} = a\left(\frac{x}{M} - \frac{x_0}{M}\right)^{-n} \tag{4}$$

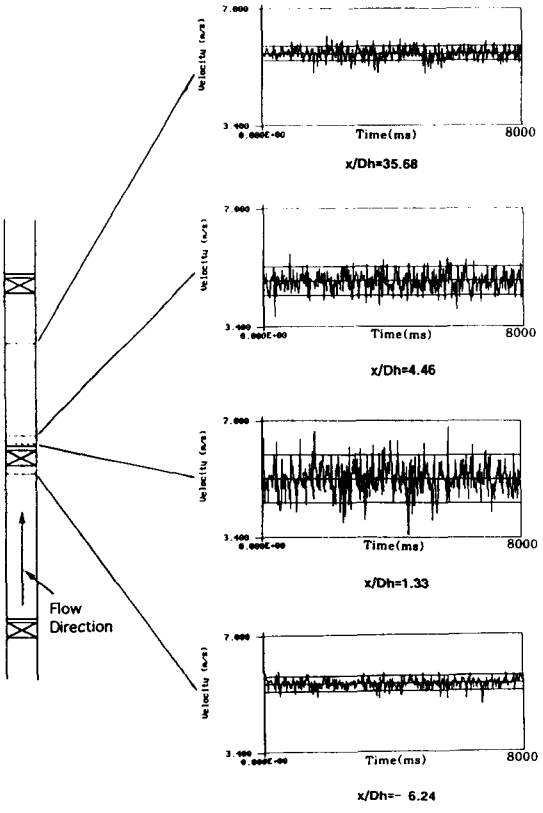

Fig. 14. Time History of Turbulent Velocity at Point 5

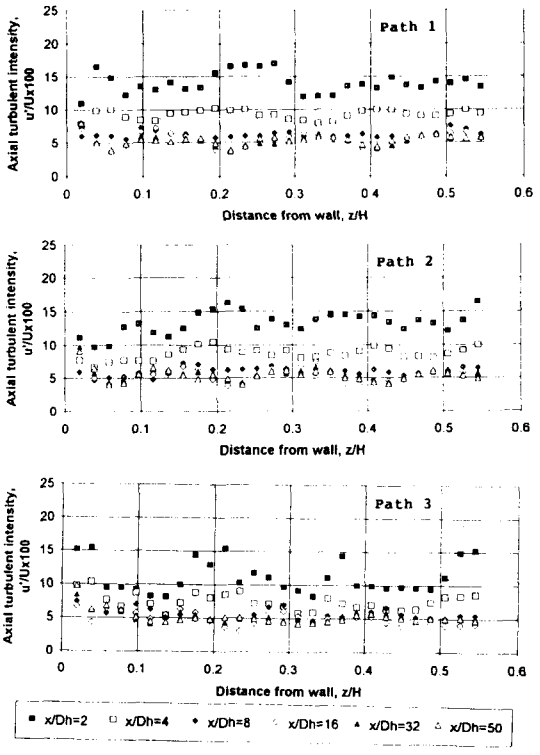

Fig. 15. Axial Turbulent Intensity Distribution at Path 1~3

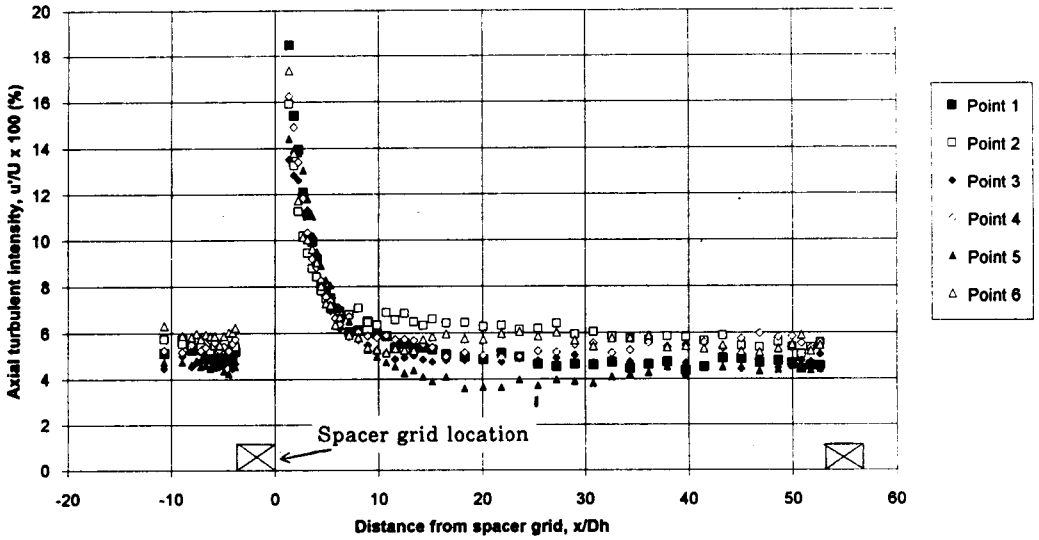

Fig. 16. Axial Turbulent Intensity Distribution at Points 1~6

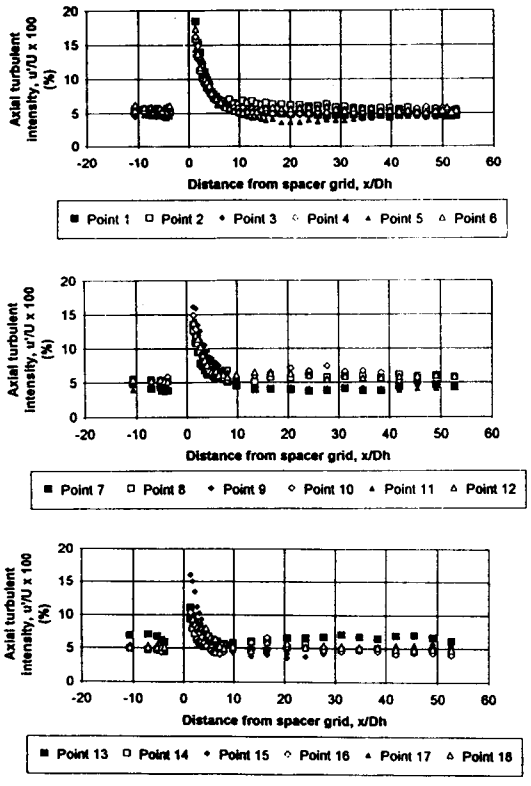

Fig. 17. Axial Turbulent Intensity Distribution at Points 1~18

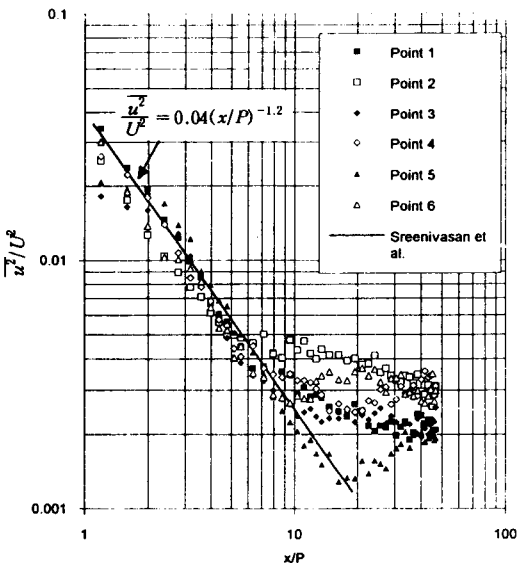

Fig. 18. Axial Turbulent Intensity Decay behind Spacer Grid at Points 1~6

where α, M, x_0, and n are fitting constant, grid mesh size, virtual origin, and decay rate, respectively. Grid mesh size, M is assumed to be pitch length, P in the present study. The axial turbulent intensities at Points 1~18 behind spacer grid are plotted in Figs.

18~20, and compared with the Sreenivasan et al.'s data[14]. For the case of Sreenivasan et al., the values of α, x_0/M, n are 0.04, 3 and 1.2, respectively. However, the virtual origin, x_0/M, of the correlation compared with the present work in Figs. 18~20 was shifted from 3 to 0. The values deviate from the correlation in Path 2 and more so in Path 3. It is generally observed that the turbulent intensity decay at Points inner region behaves as that of the mesh grid.

Some observations from the results of axial turbulence decay can be deduced by referring to conservation equation of axial turbulent intensity in steady state, constant density and three-dimensional condition.

$$U\frac{\partial \overline{u^2}}{\partial x}+V\frac{\partial \overline{u^2}}{\partial y}+W\frac{\partial \overline{u^2}}{\partial z}=$$

I

$$-2\overline{u^2}\frac{\partial U}{\partial x}-2\overline{uw}\frac{\partial U}{\partial y}-2\overline{uw}\frac{\partial U}{\partial z}$$

II

$$-\frac{\partial \overline{u^2}}{\partial x}-\frac{\partial \overline{u^2v}}{\partial y}-\frac{\partial \overline{u^2w}}{\partial z}$$

III

$$-\frac{2}{\rho}\frac{\partial \overline{pu}}{\partial x}+\nu\left(\frac{\partial^2 \overline{u^2}}{\partial x^2}+\frac{\partial^2 \overline{u^2}}{\partial y^2}+\frac{\partial^2 \overline{u^2}}{\partial z^2}\right)+\frac{2}{\rho}\overline{p\frac{\partial u}{\partial x}}$$

III IV

$$-2\nu\left[\overline{\left(\frac{\partial u}{\partial x}\right)^2}+\overline{\left(\frac{\partial u}{\partial y}\right)^2}+\overline{\left(\frac{\partial u}{\partial z}\right)^2}\right] \quad (5)$$

V

where the designated terms I, II, III, IV and V represent Convection, Production, Diffusion, Pressure re-distribution, and Dissipation terms, respectively. For the case of developing region, particularly immediately behind spacer grid, it is hard to explain the turbulence increase and decay. In developing region, all terms in Eq.(5) are contributing to axial turbulent intensity. Regarding the sharp increasing of the turbulence through spacer grids, notice the first term in Production in Eq.(5). As can be seen in Fig. 12, the axial velocities at Points 1, 3, and 5 decrease rapidly through spacer grid up to nearly $x/D_h=4$, which causes the first term of the Production to generate higher turbulence production. The axial velocities at

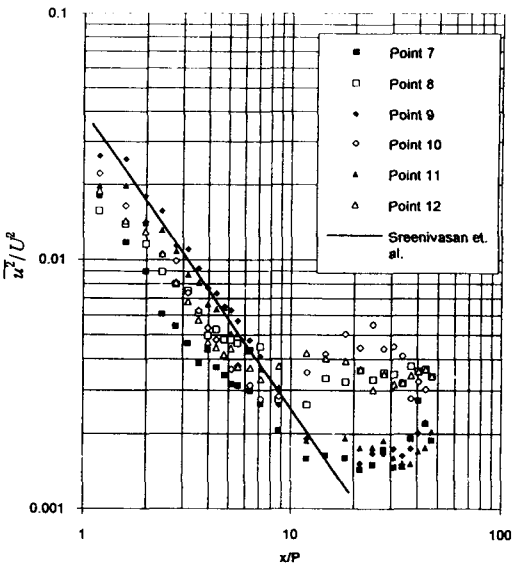

Fig. 19. Axial Turbulent Intensity Decay behind Spacer Grid at Points 7~12

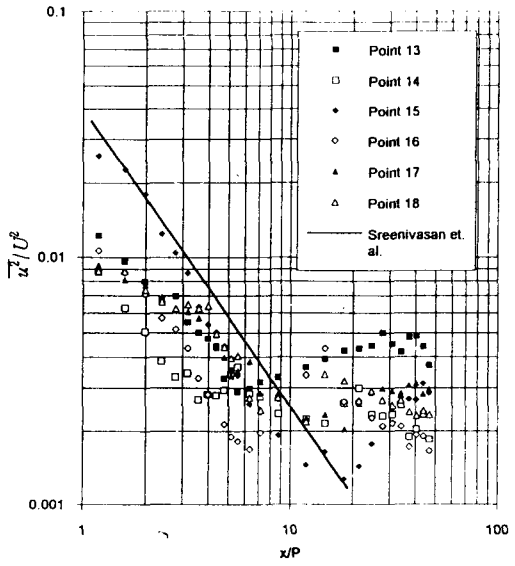

Fig. 20. Axial Turbulent Intensity Decay behind Spacer Grid at Points 13~18

2, 4, and 6 increase through spacer grid, which means that the first term of the Production generates the negative-production. This fact is indicating that at points 2, 4, and 6, V, W, velocities as well as Pressure re-distribution are dominantly contributing to axial turbulent intensity. Considering the fully developed flow, x-derivatives, V and W become 0. In this case, the second and third terms in Production and Dissipation are dominant.

3.4. Higher Moments of Velocity Fluctuation

The skewness factor, S, and flatness factor, F, which are third and fourth moment of tubulent fluctuation, are defined as [16]:

$$S=\frac{\overline{u^3}}{(u')^3} \tag{6}$$

$$F=\frac{\overline{u^4}}{(u')^4} \tag{7}$$

S and F at Points 1~18 are shown in Figs. 21 and 22. The reference values, S, and F for the Gaussian normal distribution are 0 and 3, respectively. For skewness factor, the fluctuation distribution is skewed upstream of the spacer grid, however just behind the spacer grid after passing through spacer grids, skewness factors are tended to be normal values. This implies that the turbulent flow becomes more isotropic through spacer grids. By Townsend[17], the skewness factor is related to the turbulent energy convection from larger turbulent regions to smaller turbulent regions. The flow far downstream region is strongly non-isotropic due to complex flow passage, which causes the flow region to be non-homogenious in turbulent energy and to be deviated from normal values of skewness factor. By Townsend[17], the flatness factor is related to intermittency. The effects relating to flatness factor are more pronounced the greater the difference in sizes between the energy containing eddies and the viscous eddies that dissipate the turbulent energy. In the present flow, because of non-isotropic and complex flow behavior such as inter-mixing between subchannels, the flatness factors show higher values than the normal value and some scattering values. The effects of the spacer grid on the flatness factor are not so pronounced in the results.

3.5. Implications Regarding Turbulent Thermal Mixing

Thermal hydraulic behavior of the fluid at the spacer grid is hard to analyze in detail due to the complex geometry[18]. In a possible way to approach this problem, the relation between heat and momentum transfer in turbulent flow can give information on the thermal behavior near spacer grid. Yao et al. [18] studied heat transfer augmentation by straight

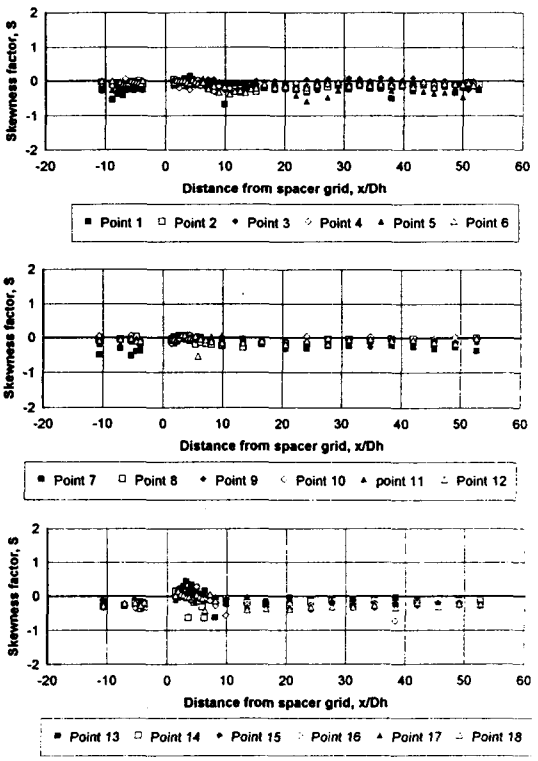

Fig. 21. Skewness Factor at Points 1~18

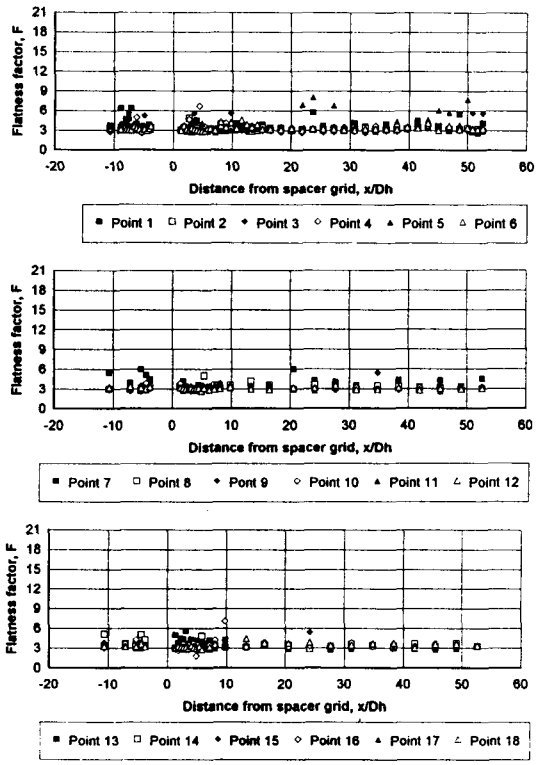

Fig. 22. Flatness Factor at Points 1~18

grid spacers in rod bundles. For single phase flow and for post-critical heat flux dispersed flow, the local heat transfer at a straight spacer and its upstream and downstream locations were treated. The highest local heat transfer is observed near the spacer grid, and downstream of the spacer grid, the heat transfer augmentation rapidly decays with x/D_h exponentially. In the present study, some quantitative values of turbulent thermal mixing which significantly contributes to the heat transfer augmentation near spacer grid were evaluated as follows.

Consider thermal energy balance in subchannels as schematically shown in Fig. 23 cited from Stewart et al. [19]. Energy conservation equation is given as

$$A\frac{\partial}{\partial t}\ll\rho h\gg_v+\frac{\partial}{\partial x}\langle\rho uh\rangle_A+\{D^T{}_C\}\{\langle\rho vh\rangle_s s\}=$$

Qcv

$$\{D^T{}_r\}[P\phi H][D_r]\{T\}$$

Qr

$$+\{D_W\}^T[LH][D_W]\{T\}$$

Qw

$$+\frac{\partial}{\partial x}A\langle x\frac{\partial T}{\partial x}\rangle_A-\{D^T{}_C\}[\frac{SC\langle x\rangle}{L_C}][D_C]\{T\}$$

Qc

$$-\{D^T{}_C\}[m_{ij}{}']\{D_C\}\{x'\} \quad (8)$$

Qt

where the designated terms Qcv, Qr, Qw, Qc, Qt represent Convection Heat Transfer to V, Heat Transfer to V from Rod, Heat Transfer to V from Wall, Conduction Heat Transfer to V, and Turbulent Heat Transfer to V, respectively. Most of detailed notations in each term are described in Ref. 19. Present study is focusing on the turbulent heat transfer, Qt in Eq.(8). The lateral thermal energy exchanges at a gap are based on a fluctuating mass exchange between neighboring subchannels. The heat transport through the gap per unit length can be expressed as

$$q_{ij}=m_{ij}{}'C_p(T_i-T_j) \quad (9)$$

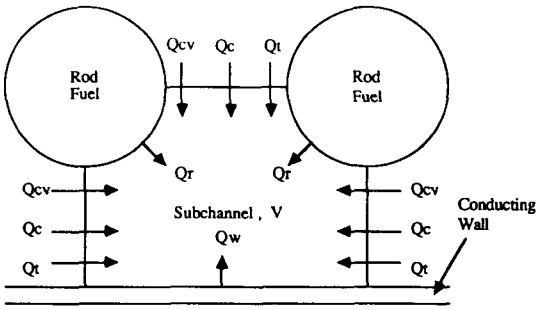

Energy Balance Equation

Qcv = Qr + Qw + Qc + Qt

Qcv = Convection Heat Transfer To V
Qr = Heat Transfer To V From Rod
Qw = Heat Transfer To V From Wall
Qc = Conduction Heat Transfer To V
Qt = Turbulent Heat Transfer To V

Fig. 23. Schematic Diagram of Energy Balance

where T_i, T_j and m_{ij}' are the bulk temperatures of two adjacent subchannels i and j, and the fluctuating cross-flow mixing rate per unit length between subchannels, respectively. m_{ij}' is defined as[19]

$$m_{ij}' = \rho w_{eff} s \tag{10}$$

where w_{eff} and s are the effective mean mixing velocity and rod gap spacing, respectively. If the enthalpies and velocities of the neighboring subchannels are different, an exchange of energy and momentum flux will occur. The expressions for the net turbulent energy flux, F_h, and momentum flux, F_m, between subchannels can be given, respectively, by [19]

$$F_h = \rho w_{eff} \Delta h \tag{11}$$

and

$$F_m = F_t \rho w_{eff} \Delta U \tag{12}$$

where Δh and ΔU are the average enthalpy and axial velocity difference between subchannels, and F_t is a correction factor which is related to the difference between turbulent energy and momentum transport. The turbulent cross-flow flux can be expressed as diffusive energy flux between centroids of subchannels, by introducing a mixing factor[20~23], can be given as

$$F_h = \varepsilon Y \rho \frac{\Delta h}{\Delta y} \tag{13}$$

where ε, Y and Δy are, respectively, the reference turbulent eddy viscosity, a mixing factor and the centroid or mixing distance between subchannels. Ingesson and Hedberg[24] used the eddy viscosity at the center of a circular tube as a reference eddy viscosity, i.e.,

$$\varepsilon = \nu (f_c/8)^{0.5} Re/20 \tag{14}$$

where f_c and υ are the friction factor of a circular tube and a kinematic viscosity of a fluid, respectively. Equating Eq.(11) to Eq.(13) yields

$$Y = w_{eff} \Delta y / \varepsilon \tag{15}$$

Moller[20] obtained the mixing velocity by supposing that the dominant frequency eddies are responsible for the turbulent mass flow exchange between the gaps. However, in the present study, we considered that all the different size eddies are contributing for turbulent cross-flow mass exchange. This consideration led to that effective mixing velocity, weff, equals to the azimuthal turbulent velocity, w'. However, weff is not available in the present measurement, weff/weff(far downstream) = u'/u'(far dwonstream), was assumed at the central region in the gap. This assumption is valid in the present P/D ratio range by referring to Trupp and Azad[25] and Rehme[3]. In Fig. 24, local mixing factor, Y, nondimensionalized by that far downstream, Y_o, was obtained and compared with the local heat transfer rate[18] , Nu, nondimensionalized by that far downstrem, Nu_o. Mixing factors show the highest value near spacer grid and they decrease rapidly up to about $x/D_h = 15$. A fitted correlation for mixing factors was obtained as

$$Y/Y_o = 1 + 3.97558 e^{-0.387(x/D_h + 0.57)} \tag{16}$$

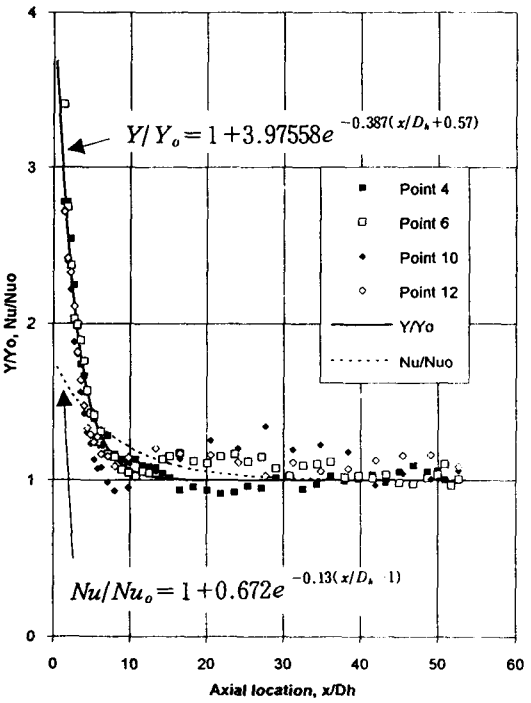

Fig. 24. Local Mixing Factor Compared with Local Nusselt Number

This correlation is compared with that of local Nusselt number in Ref. 18 for the spacer grid with the nearly same blockage ratio as the present. Local Nusselt number correlation is given as

$$Nu/Nu_o = 1 + 0.672e^{-0.13(x/D_h - 1)} \quad (17)$$

The tendency between mixing factors and Nusselt number is the same. Both of them, near spacer grid, decays rapidly with x/D_h exponentionally. As a matter of fact, mixing factors are not compared with local Nusselt number quantitatively, since local Nusselt number is global phenomena in a flow cross-section. Thermal phenomena in entire subchannels are governed by various contributing factors, i.e. forced convective, conductive, and turbulent mixing heat transfer etc.

4. Concluding Remarks

In order to investigate the effects of mixing spacer grid on the turbulence in rod bundles, the detailed hydraulic characteristics in subchannels of 5×5 rod bundles with mixing spacer grids were measured by using an LDV(laser Doppler Velocimeter). The experimental results led to the following conclusions.

It was generally observed that the turbulent intensity decay rates behind the spacer grid can be explained by turbulence decay in turbulent flow through mesh grids or screens, and show similar trends as mesh grid or screen flows. The flow immediately behind the spacer grid is intensively fluctuating with a higher turbulence energy and more isotropic than just before the spacer grid.

For skewness factor, the fluctuation distribution is skewed upstream of the spacer grid, however just behind the spacer grid after passing through spacer grids, skewness factors are tended to be normal values. The effects of the spacer grid on the flatness factor are not so pronounced in the results.

A mixing factor correlation was generated and compared with that of nondimensionalized Nusselt numbers. Finally, the spacer grids actively affect the turbulent flow of rod bundles up to about $x/D_h = 20$ and are significantly influencing the thermal mixing.

Acknowledgements

The test bundles were assembled with Zircaloy tubes obtained from KNFC and spacer grids of Siemens type provided by Nuclear Fuel Design Group at KAERI. The authors wish to express their appreciation to them.

Nomenclatures

D	rod diameter, m
D_h	hydraulic diameter, m
F_h	net turbulent energy flux, J/(m²s)
F_m	momentum flux, kg/(ms²)
F_t	correction factor
f	friction factor
f_D	Doppler shift frequency, 1/s
h	enthalpy, J/kg
Δh	enthalpy difference between subchannels, J/kg
P	pitch, m
p	pressure, Pa
Re	Reynolds number (U_{av} D_h/υ), dimensionless
s	rod gap spacing, m
U	axial time mean velocity, m/s
ΔU	velocity difference between subchannels, m/s
U_{av}	entire subchannel average velocity, m/s
$\tilde{u}$	instantaneous velocity, m/s
u	axial fluctuating velocity, m/s
u′	root mean square of u m/s
V	subchannel control vol ume in Fig. 23
V	radial time mean velocity, m/sec
v	radial fluctuating velocity, m/s
W	wall distance, m
W	azimuthal time mean velocity, m/sec
w	azimuthal fluctuating velocity, m/s
w′	root mean square of w, m/sec
x	axial coordinate, m
Y	mixing factor
y	traversing coordinate, m

Δy centroid or mixing distance between subchannels, m

z traversing coordinate, m

Greek Symbols

ε turbulent eddy viscosity, m^2/s

x half angle of laser beam intersection, Degree

λ laser wavelength, m

v kinematic viscosity, m^2/s

σ fluid density, kg/m^3

References

1. D.S. Rowe, B.M. Johnson, and J.G. Knudsen, " Implications Concerning Rod Bundle Cross-flow Mixing Based on Measurements of Turbulent Flow Structure," Int. J. Heat Mass Transfer, 17, 407−418 (1974)
2. K. Rehme, "Distribution of Velocity and Turbulence in a Parallel Flow along an Asymmetric Rod Bundle," Nucl. Technol., 15, 148−159 (1982)
3. K. Rehme, "The Structure of Turbulent Flow through Rod Bundles," Nucl. Engrg. Des. 99, 1141−154 (1987)
4. J.D. Hooper, and K. Rehme, "Large-Scale Structure Effects in Developed Turbulent Flow through Closely-Spaced Rod Arrays," J. Fluid Mech., 145, 305-337 (1984)
5. V. Vonka, "Measurement of Secondary Flow Vortices in a Rod Bundle," Nucl. Eng. Des., 106, 191−207 (1988)
6. K. Rehme, "Pressure Drop Correlation for Fuel Element Spacers," Nucl. Technol. Vol. 17, 15−23 (1973)
7. D.S. Rowe and C.C. Chapman, "Measurement of Turbulent Velocity, Intensity and Scale in Rod Bundle Flow Channels Containing a Grid Spacer," BNWL-1757 (1973)
8. K. Rehme and G. Trippe, "Pressure Drop and Velocity Distribution in Rod Bundles with Spacer Grids," Nucl. Engrg. and Des. 62, 349−359 (1980)
9. Y.F. Shen, Z.D. Cao and Q.G. Lu, "An Investigation of Crossflow Mixing Effect Caused by Grid Spacer with Mixing Blades in a Rod Bundle," Nucl. Engrg. and Des.,Vol. 125, 111−119 (1991)
10. F. Durst, A. Melling and J.H. Whitelaw, Principles and Practice of Laser Doppler Anemometry, Academic Press (1976)
11. L.E. Drain, The Laser Doppler Technique, John Wiley and Sons (1980)
12. H. Blasius, The Law of Similarity for Frictional Processes in Fluids (originally in German), Forsch Arb. Ing.−Wesen(Berlin) (1913)
13. G. Comte-Bellot and S. Corrsin, "The Use of a Contraction to Improve the Isotropy of Generated Turbulence," J. Fluid Mech. Vol. 25, part4, pp. 657−682 (1966)
14. K.R. Sreenivasan et al., "Temperature Fluctuations and Scales in Grid-generated Turbulence," J. Fluid Mech. , Vol. 100, part 3, 597−621 (1980)
15. E.M. Laws and J.L. Livesey, "Flow through Screens," Annual Review of Fluid Mechanics, Vol. 10 (1978)
16. H. Tennekes and J.L. Lumley, The First Course in Turbulence, MIT Press, Cambridge, Mass. (1972)
17. A.A. Townsend, The Structure of Turbulent Shear Flow, Cambridge University Press (1976)
18. S.C. Yao, L.E. Hochreiter and W.J. Leech, "Heat Transfer Augmentation in Rod bundles near Grids," J. of Heat Transfer, Trans. of the ASME, Vol. 104, 76−81 (1982)
19. C.W. Stewart, C.L. Wheeler, R.J. Cena, C.A. Mamonagle, J.M. Cuta, and D.S. Trent, COBRA-IV: The Model and the Method, Battelle, Pacific Northwest Laboratories (1977)
20. S.V. Moller, "Single-phase Turbulent Mixing in

Rod Bundles," Experimental Thermal and Fluid Science, 5, 26−33 (1992)

21. K. Rehme, "The Structure of Turbulence in Rod Bundles and the Implications on Natural Mixing between the Subchannels," Int. J. Heat Mass Transfer, Vol. 35, No. 2, 567−581 (1992)
22. X. Wu, and A.C. Trupp (1994), "Spectral Measurements and Mixing Correlation Simulated Rod Bundles Subchannels," Int. J. Heat Mass Transfer, Vol. 37, Vol. 8, 1277−1281 (1994)
23. S.K. Yang and M.K. Chung, "Turbulent Flow through Mixing Spacer Grids in Rod Bundles," HTD-Vol. 316, National Heat Transfer Conference, Vol. 14, 33−40 (1995)
24. L. Ingesson and S. Hedberg, Heat Transfer between Subchannels in a Rod Bundle, Heat transfer (1970), Paris, Vol. Ⅲ, Fc 7. 11, Elsevier (1970)
25. A.C. Trupp and R.S. Azad, "The structure of Turbulent Flow in Triangular Array Rod Bundles," Nucl. Engr. Des. 32. 47−84 (1975)